nature communications

Article

https://doi.org/10.1038/s41467-025-67881-4

Discovery of high-temperature charge order and time-reversal symmetry-breaking in the kagome superconductor YRu_3Si_2

Received: 10 June 2025

Accepted: 10 December 2025

Published online: 21 December 2025

Check for updates

P. Král[1,9], J. N. Graham[1,9], V. Sazgari[1,9], I. Plokhikh[1,2], A. Lukovkina[3], O. Gerguri[1], I. Biało[4], A. Doll[1], L. Martinelli[4], J. Oppliger[4], S. S. Islam[1], M. Spitaler[1], K. Wang[5], M. Salamin[3], H. Luetkens[1], R. Khasanov[1], M. V. Zimmermann[6], J.-X. Yin[7], Ziqiang Wang[8], J. Chang[4], B. Monserrat[5], D. Gawryluk[1], F. O. von Rohr[3], S.-W. Kim[5] ✉ & Z. Guguchia[1] ✉

Identifying high-temperature unconventional charge order and superconductivity in kagome systems is crucial for understanding frustrated, correlated electrons and enabling future quantum technologies. Here, we report that the kagome superconductor YRu_3Si_2 hosts an exceptional interplay of charge order, magnetism, and superconductivity, revealed through a comprehensive suite of muon spin rotation (μSR), magnetotransport, X-ray diffraction, and density functional theory (DFT). We identify a high-temperature charge-ordered state with propagation vector (1/2,0,0) and a record onset temperature of 800 K, unprecedented in kagome systems and quantum materials more broadly. μSR measurements further reveal time-reversal symmetry-breaking below 25 K and field-induced magnetism near 90 K, features mirrored in the magnetoresistance, which reaches 45% at low temperatures. Band-structure calculations show two van Hove singularities near the Fermi level, including one within a flat band. At low temperatures, YRu_3Si_2 becomes superconducting below T_c = 3.4 K with either two full isotropic gaps or an anisotropic nodeless gap. These results establish YRu_3Si_2 as a prime platform for studying correlated kagome physics.

Identifying novel quantum phases and emergent electronic transitions—especially those intertwined with superconductivity at elevated temperatures—remains one of the central pursuits in condensed matter physics[1]. The interplay between symmetry breaking, electronic correlations, and topology often gives rise to unconventional states of matter with potential relevance for quantum technologies. Among the diverse platforms studied, kagome lattice systems have recently garnered significant attention as fertile ground for realizing such exotic phenomena.

The kagome lattice[2], with its geometrically frustrated network of corner-sharing triangles, hosts a unique band structure characterized by Dirac crossings, flat bands, and van Hove singularities (VHSs), making it an ideal setting to explore the interplay of electronic topology, magnetism, and superconductivity. A growing family of

[1]PSI Center for Neutron and Muon Sciences, Villigen, Switzerland. [2]TU Dortmund University, Department of Physics, Dortmund, Germany. [3]Department of Quantum Matter Physics, University of Geneva, Geneva, Switzerland. [4]Physik-Institut, Universität Zürich, Zürich, Switzerland. [5]Department of Materials Science and Metallurgy, University of Cambridge, Cambridge, UK. [6]Deutsches Elektronen-Synchrotron, Hamburg, Germany. [7]Department of Physics, Southern University of Science and Technology, Shenzhen, Guangdong, China. [8]Department of Physics, Boston College, Chestnut Hill, MA, USA. [9]These authors contributed equally: P. Král, J. N. Graham, V. Sazgari. ✉e-mail: swk38@cam.ac.uk; zurab.guguchia@psi.ch

kagome metals—including AV_3Sb_5 (A = K, Rb, Cs), $CsCr_3Sb_5$, $CsTi_3Bi_5$, ScV_6Sn_6, FeGe, and $Ta_2V_{3.1}Si_{0.9}$—has exhibited a wealth of correlated behaviors[3–25], such as charge order (CO), nematicity, time-reversal symmetry (TRS) breaking[8,19,26], and unconventional superconductivity. These findings underscore the potential of the kagome lattice as a platform that hosts emergent quantum phenomena.

Within this landscape, $LaRu_3Si_2$[10,27–32] has recently attracted attention due to its rich physics. It exhibits charge order with a record onset temperature of 400 K[10], followed by a secondary charge order with field-induced magnetism below 80 K and TRS breaking below 35 K[29]. High-pressure studies on $LaRu_3Si_2$ by our group[30] and others[33] reveal a dome-shaped superconducting phase and a similar trend in the normal-state electronic response, suggesting unconventional pairing and a positive correlation between superconductivity and normal-state electronic behavior. These features distinguish it from other kagome materials and motivate the exploration of related compounds within the same structural family.

To further understand the kagome 132 systems, one promising approach is to apply chemical pressure—for example, by substituting La with the smaller Y ion, resulting in YRu_3Si_2. While YRu_3Si_2 retains the same crystal structure, its superconducting transition temperature ($T_c \simeq 3.4$ K)[34] is roughly half that of $LaRu_3Si_2$. This raises fundamental questions about the origin of superconductivity and its interplay with other ordering phenomena in this material class. It is therefore of great interest to explore the microscopic nature of superconductivity in YRu_3Si_2, particularly focusing on the superfluid density and the symmetry of the superconducting gap. Even more crucially, we seek to determine whether charge order—a prominent feature of $LaRu_3Si_2$—also emerges in YRu_3Si_2, and how its presence or absence may be linked to the observed suppression of T_c. Gaining such insights is vital for deepening our understanding of intertwined electronic orders in kagome superconductors and for guiding the discovery and design of new materials with tunable quantum phases.

In this article, we report the discovery of charge order in YRu_3Si_2 with a propagation vector of (1/2, 0, 0) and a record onset temperature of 800 K, alongside field-induced magnetism below 90 K and time-reversal symmetry (TRS) breaking below 25 K. DFT calculations reveal a characteristic kagome band structure featuring two van Hove singularities near the Fermi level, one of which lies within a flat band. Bulk superconductivity emerges below 3.4 K, with a two-gap (s + s)-wave or anisotropic s-wave pairing symmetry. These findings demonstrate a rare coexistence of charge order, magnetism, and multigap superconductivity, establishing YRu_3Si_2 as a model system for correlated kagome physics.

Results

Structural evolution and charge order from X-ray diffraction and DFT

Firstly, to determine the presence of charge order, X-ray diffraction (XRD) experiments on YRu_3Si_2 were conducted over a temperature range of 80 to ~900 K. The reconstructed reciprocal patterns obtained at various temperatures are shown in Fig. 1a–h. Above 800 K, we identified the *Cccm* structure, the same phase as observed in $LaRu_3Si_2$[10] between 400 and 600 K. Below 800 K, down to 10 K, superstructure reflections emerge, which in the hexagonal setting correspond to $\mathbf{q}_1 = (1/2, 0, 0)$, $\mathbf{q}_2 = (0, 1/2, 0)$, and $\mathbf{q}_3 = (1/2, -1/2, 0)$. In the orthorhombic setting, these reflections indicate a breaking of the *C*-centering, signifying a structural transition from *Cccm* to *Pmma*. This transition establishes charge order at $T_{co} = 800$ K in YRu_3Si_2, which is twice as high as in $LaRu_3Si_2$ ($T_{co} = 400$ K), setting a new record for charge order in kagome systems-and in quantum materials more broadly. Note that, unlike in the case of $LaRu_3Si_2$, the *P6/mmm* (HT-HEX) was not observed experimentally up to the highest temperature used in our measurements. Nevertheless, the presence of hexagonal symmetry in the diffraction pattern and the need to invoke hexagonal twin domains for structure refinement suggest the existence of a high-temperature phase with hexagonal symmetry, a conclusion further supported by the DFT calculations presented in the following paragraph. To avoid ambiguity, we clarify here the notation used throughout this manuscript for the different structural phases. In our previous work for $LaRu_3Si_2$[10], we adopted the designations LT-HEX and HT-HEX for the *Cccm* and *P6/mmm* phases, respectively. This choice is motivated by the fact that the diffraction patterns (Laue symmetry) of both phases display hexagonal

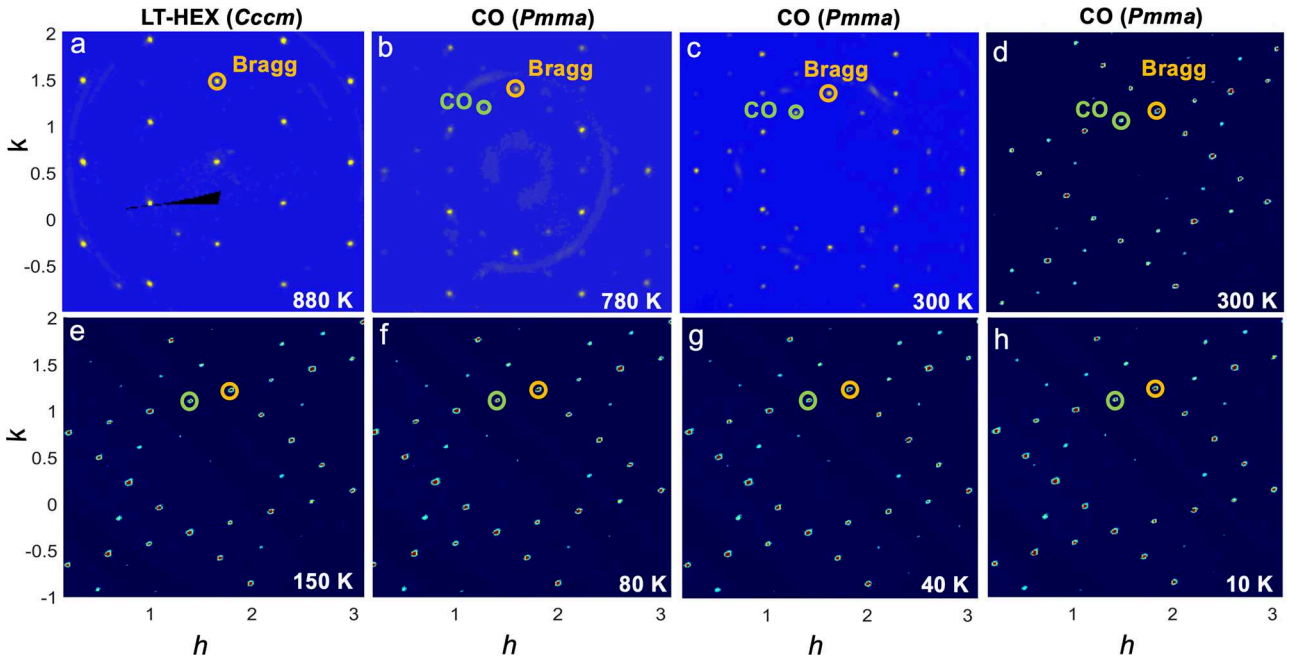

Fig. 1 | Above room temperature charge order in YRu_3Si_2. Reconstructed reciprocal space along the (0 0 1) direction at 2 r.l.u. (reciprocal lattice units), performed at various temperatures $T = 880$ K (**a**), 780 K (**b**), 300 K (from laboratory single crystal X-ray diffraction) (**c**), 300 K (from synchrotron X-ray diffraction) (**d**), 150 K (**e**), 80 K (**f**), 40 K (**g**), and 10 K (**h**), respectively. Orange and green circles mark the Bragg peak and charge order (CO) peaks, respectively.

https://doi.org/10.1038/s41467-025-67881-4

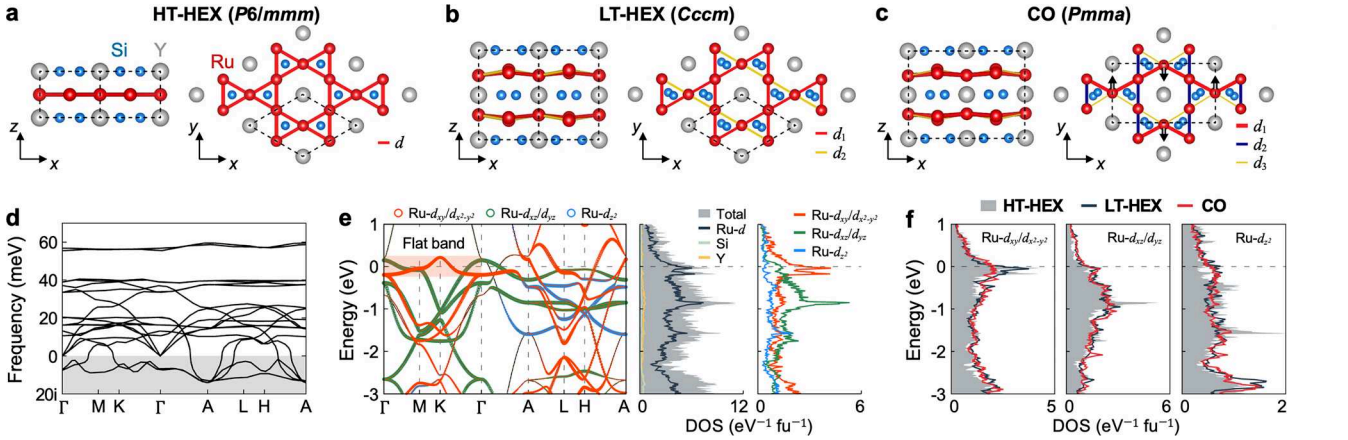

Fig. 2 | Electronic structure and density of states in YRu_3Si_2. Atomic structures of **a** HT-HEX (*P6/mmm*), **b** LT-HEX (*Cccm*), and **c** CO (*Pmma*) phases in YRu_3Si_2. Dashed lines indicate the unit cells. In each structure, Ru–Ru bonds of different lengths are depicted in different colors. In **c**, black arrows in the right panel show the in-plane CO displacement patterns of Ru atoms. **d** Phonon dispersion of the HT-HEX structure. **e** Orbital-projected band structure and density of states (DOS) of the HT-HEX structure. The *d* orbitals of Ru atoms are projected onto the band structure, with the radius of the open circles proportional to the projected weight. **f** Orbital-projected DOS of the three structures.

symmetry, despite their underlying crystal structures being different. Structural refinement reveals that the true crystal symmetry is lower than the Laue symmetry due to the formation of twin domains oriented according to the high-temperature phase. For consistency with our earlier work on $LaRu_3Si_2$[10], we continue to use the LT-HEX notation for the *Cccm* phase, which for YRu_3Si_2 is stable up to 880 K, and HT-HEX for the *P6/mmm* phase.

To gain a more detailed insight into the distortions and phase stability of YRu_3Si_2, first-principles DFT calculations have been performed. Our calculations identify the experimentally observed *Cccm* and *Pmma* structures, and we consider their parent high-temperature *P6/mmm* structure (Fig. 2a–c). The parent structure *P6/mmm* is characterized by an undistorted kagome lattice of Ru atoms. In this high-symmetry phase, all Ru–Ru bonds are equivalent with length d, reflecting a uniform distribution of electron density with no preferred direction or site disproportionation. The *P6/mmm* structure exhibits multiple unstable imaginary modes across the whole BZ in its phonon dispersion (Fig. 2d). The imaginary phonon mode at the A point gives rise to the *Cccm* structure characterized by in-plane displacements of Si atoms and out-of-plane displacements of Ru atoms. The out-of-plane modulation yields two different bond lengths in the Ru kagome net, $d_1 = 2.759$ Å and $d_2 = 2.793$ Å, both of which are larger than $d = 2.736$ Å in the parent *P6/mmm* structure. Because all bonds expand uniformly, this change indicates a simple structural phase transition rather than the formation of charge order. This distortion lifts peaks in the density of states (DOS) of the out-of-plane d_{xz}, d_{yz}, and d_{z^2} orbitals far below the Fermi level (Fig. 2f). The large DOS at the Fermi level, originating from the flat band of the in-plane d_{xy} and $d_{x^2-y^2}$ orbitals (Fig. 2e), remains nearly unchanged upon the distortion. For the *Pmma* structure, the structural distortion arises from imaginary phonon modes at A and L points, featuring in-plane Ru distortions (see arrows in Fig. 2c) in addition to in-plane Si distortions and out-of-plane Ru distortions. In the distorted *Pmma* structure, the Ru–Ru bonds split into three distinct lengths: $d_1 = 2.708$ Å, $d_2 = 2.760$ Å, and $d_3 = 2.833$ Å. Notably, d_1 is shorter than the uniform Ru–Ru bond length d in the *P6/mmm* phase. The contraction of a subset of bonds relative to the parent value ($d_1 < d$) indicates that the electronic charge density is no longer uniformly distributed, but instead becomes preferentially localized along specific Ru–Ru links. This bond disproportionation is not a mere structural byproduct; rather, it reflects an underlying electronic instability in which certain Ru–Ru pairs host enhanced charge density, while others are depleted. In essence, the lattice distortion enforces a periodic modulation of electron density—commonly referred to as charge order. This phenomenon is analogous to the Peierls distortion in a one-dimensional chain, where uniform bonds alternate into short and long distances; the short bonds signify enhanced charge density (dimerization), thereby stabilizing the charge-ordered state. The charge order nature of the *Pmma* structure is further confirmed by the reduction in the large DOS, originating from the flat band of the in-plane d_{xy} and $d_{x^2-y^2}$ orbitals at the Fermi level, compared to the parent *P6/mmm* structure (Fig. 2f).

Magnetotransport properties in the superconducting and normal states

Having observed charge order and confirmed it through DFT calculations, we next investigate the transport characteristics in both the superconducting and normal states. The temperature dependence of electrical resistivity for YRu_3Si_2 is shown Fig. 3a. The resistivity exhibits metallic behavior in the charge-ordered state, similar to that observed in $LaRu_3Si_2$[29] and in the kagome superconductors AV_3Sb_5[4]. This indicates that the charge order in YRu_3Si_2 reconstructs the Fermi surface only partially, leaving a substantial number of metallic carriers intact. As a result, transport remains dominated by ungapped bands and resistivity decreases with decreasing temperature, rather than showing an increase. Such behavior is typical of multiband or three-dimensional systems, in contrast to low-dimensional Peierls systems, where charge order strongly gaps the Fermi surface and drives resistivity upward. $\rho(T)$, depicted in Fig. 3a establishes three temperature scales governing the electronic behavior. Inspecting the first derivative of the resistivity data reveals a subtle change in slope at $T_1^{*(R)} \sim 90\,K$, followed by a pronounced peak at $T_2^{*(R)} \sim 35\,K$. These values are comparable to $T_{CO,II} \simeq 80$ K and $T^* \simeq 35$ K observed in $LaRu_3Si_2$. In the low-temperature range, the superconducting state is reached with the onset and midpoint (50% drop in resistivity) at 3.9 and 3.7 K, respectively. Superconducting transitions under varying magnetic fields are presented in the color plot, with temperature on the vertical axis and magnetic field on the horizontal axis. Blue regions represent the zero-resistance superconducting state, while red regions correspond to the normal (resistive) state. The application of a magnetic field results in the gradual suppression of the transition temperature (Fig. 3b) with an estimated upper critical field $\mu_0 H_{c2} = 1.0$ T at $T = 2$ K. Motivated by the presence of two distinct temperature scales observed in the normal state via the resistivity derivative, magnetoresistance (MR) was measured across a broad range of temperatures and magnetic fields. The resulting data, displayed in the color plot (Fig. 3d), reveal that MR emerges below ~80 K and reaches up to 45%. The temperature

https://doi.org/10.1038/s41467-025-67881-4

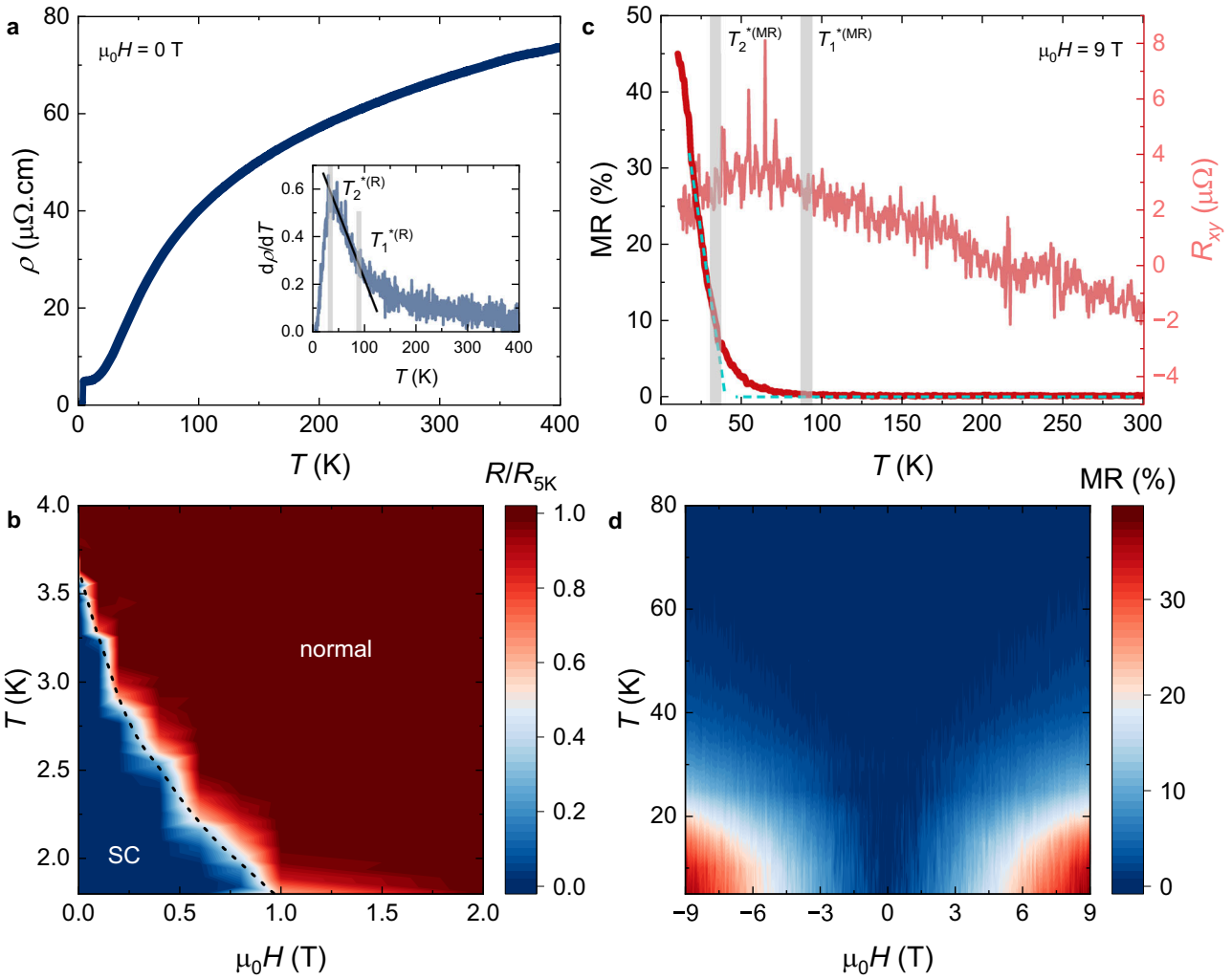

Fig. 3 | Magnetotransport characteristics for YRu_3Si_2. a Temperature dependence of electrical resistivity and its first derivative (inset). **b** Contour map of the resistivity data across the superconducting transition as a function of applied magnetic field. **c** Temperature-dependent magnetoresistance (left axis), and the Hall resistance (right axis) obtained at 9 T. Vertical gray lines in **a** and **c** mark the characteristic temperatures. **d** Temperature-field contour map of magnetoresistance.

dependence of the MR measured at 9 T is presented in Fig. 3c. Two clear slope changes are observed, showing the initial deviation from zero MR below $T_1^{*(MR)}$ with a significant increase below $T_2^{*(MR)}$, which coincides with the values determined from the derivative of resistivity. Additionally, the temperature dependence of the Hall resistivity shows a broad anomaly in the corresponding temperature range. Our MR experiments therefore indicate the presence of a transition or crossover in the normal state, occurring between the onset of charge order and the emergence of superconductivity.

Microscopic superconducting and normal-state properties probed by μSR

In order to unveil the microscopic nature of both normal and superconducting states of YRu_3Si_2, μSR experiments were carried out. Unlike many other methods that probe the penetration depth (λ) only near the surface, the μSR technique offers a powerful means of measuring the superfluid density in the vortex state of type-II superconductors deep within the bulk of the sample. Further details are provided in the "Methods" section. Additionally, zero-field μSR can detect internal magnetic fields as small as 0.1 G without the need for an external field, making it an especially valuable tool for probing spontaneous magnetism associated with TRS breaking. Figure 4a illustrates the transverse-field (TF) μSR time spectra in an applied magnetic field of 50 mT above (3.4 K) and below (0.1 K) the SC transition. Above T_c, the oscillations show a weak damping due to the random local fields from the nuclear moments, while below T_c the damping rate strongly increases, indicating the presence of a non-uniform local magnetic field distribution due to the formation of a flux-line lattice. Further evidence is provided in Fig. 4b showing the Fourier transform of the μSR spectra at corresponding temperatures. Above T_c, a sharp and symmetric peak is observed. In the superconducting state, however, the field distribution becomes significantly broadened and asymmetric—features characteristic of a vortex lattice—and is shifted away from the applied magnetic field. The diamagnetic shift $\Delta B_{int} = \mu_0(H_{int,SC}-H_{int,NS})$, i.e., the difference between the applied field and the central field in a superconducting state, as a function of temperature, is shown in Fig. 4c. The large diamagnetic response of 1.1 mT that is observed is associated with the superconducting transition at T_c = 3.4 K. This large diamagnetic shift indicates the bulk character of superconductivity. An in-depth look at the superconducting properties is offered by the analysis of the muon spin depolarization rate $\sigma_{tot}(=\sqrt{\sigma_{SC}^2+\sigma_{nm}^2})$, consisting of superconducting, σ_{SC}, and nuclear magnetic dipolar, σ_{nm}, contributions. To estimate the superconducting relaxation rate σ_{SC}, the nuclear contribution was considered to be constant above T_c and

https://doi.org/10.1038/s41467-025-67881-4

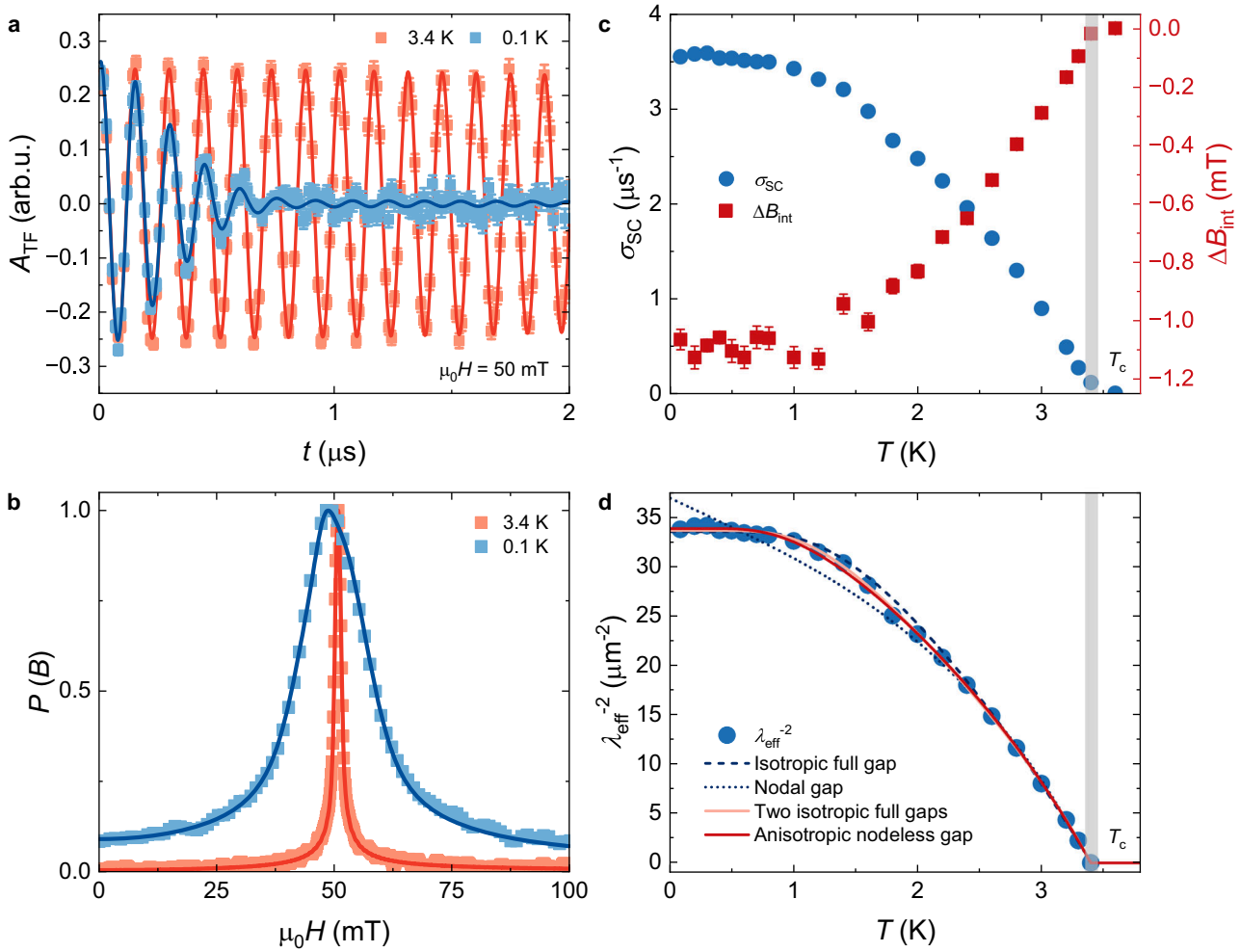

Fig. 4 | Superconducting-state properties of YRu_3Si_2 probed by μSR. **a** Transverse field (TF) μSR time spectra obtained above (3.4 K) and below (0.1 K) the SC transition under an applied magnetic field of 50 mT. The solid lines represent fits to the data by means of Eq. (2). Error bars are the standard error of the mean (s.e.m.) in about 10^6 events. **b** Normalized Fourier transform of the measured time spectra in the normal and superconducting state, respectively. **c** Temperature dependence of the muon spin depolarization rate $\sigma_{sc}(T)$ (left axis), and diamagnetic shift $\Delta B_{int}(T)$ (right axis), at 50 mT. The error bars represent the standard deviation of the fit parameters. **d** Inverse squared effective penetration depth λ_{eff}^{-2} as a function of temperature fitted with several theoretical models (see the "Methods" section).

subtracted accordingly. The temperature dependence of σ_{SC} of YRu_3Si_2 is shown in Fig. 4c, which was extracted using the equations described in the "Methods" section. The form of the temperature dependence of σ_{SC}, which reflects the topology of the SC gap, shows saturation below $T/T_c \simeq 0.3$. We show in the following how these behaviors indicate a nodeless SC gap.

For a perfect triangular lattice, the relaxation rate is directly linked to the magnetic penetration depth λ_{eff} according to the equation[35]:

$$\frac{\sigma_{SC}(T)}{\gamma_\mu} = 0.06091 \frac{\Phi_0}{\lambda_{eff}^2(T)} \quad (1)$$

where γ_μ is the gyromagnetic ratio of the muon and Φ_0 stands for the magnetic-flux quantum. The magnetic penetration depth is one of the most fundamental parameters in a superconductor since it is related to the superfluid density, n_s, via $1/\lambda^2 = \mu_0 e^2 n_s/m^*$ (where m^* is the effective mass). The temperature dependence of $1/\lambda^2$ is shown in Fig. 4d. To enable a quantitative analysis, the experimental data were fitted using theoretical models corresponding to a single isotropic full gap, two isotropic full gaps, an anisotropic nodeless gap, and a nodal gap. The fits are presented in Fig. 4d. The nodal gap model is clearly incompatible with the experimental data, and the single isotropic full-gap model also fails to adequately describe the temperature dependence of $\lambda_{eff}^{-2}(T)$. In contrast, both the two-gap isotropic model and the anisotropic nodeless gap model yield fits of comparable and satisfactory quality. The first approach suggests the presence of two SC gaps, $\Delta_1 = 0.53(1)$ meV and $\Delta_2 = 0.15(1)$ meV, with relative weights of 0.93(1) and 0.07(1). In the second scenario, the superconducting gap exhibits an angular dependence similar to that in the case of nodal d-wave superconductivity, however, without reaching the zero value at any point. The anisotropy ratio of the minimum gap value to the maximum $\Delta_1 = 0.52(1)$ meV is $a = 0.20(2)$, which is lower compared to other anisotropic s-wave kagome superconductors, e.g., $CeRu_2$[36]. The SC gap structure for the La analog, $LaRu_3Si_2$, was described by a single s-wave model[28], nevertheless, the presence of two gaps cannot be excluded, as well[37], with a similar weight ratio (0.1 and 0.9) as observed here. The magnetic penetration depth extrapolated to zero temperature is estimated to be $\lambda_{eff}(0) = 173(3)$ nm. The ratio between the superconducting critical temperature and the zero-temperature superfluid density, $T_c/\lambda_{eff}(0)^{-2}$, is ~0.10 for YRu_3Si_2, which is lower than the value of 0.37 reported for $LaRu_3Si_2$[28], but still within the typical range for unconventional superconductors (0.1–20)[38]. In contrast, conventional BCS superconductors exhibit significantly smaller values. This

https://doi.org/10.1038/s41467-025-67881-4

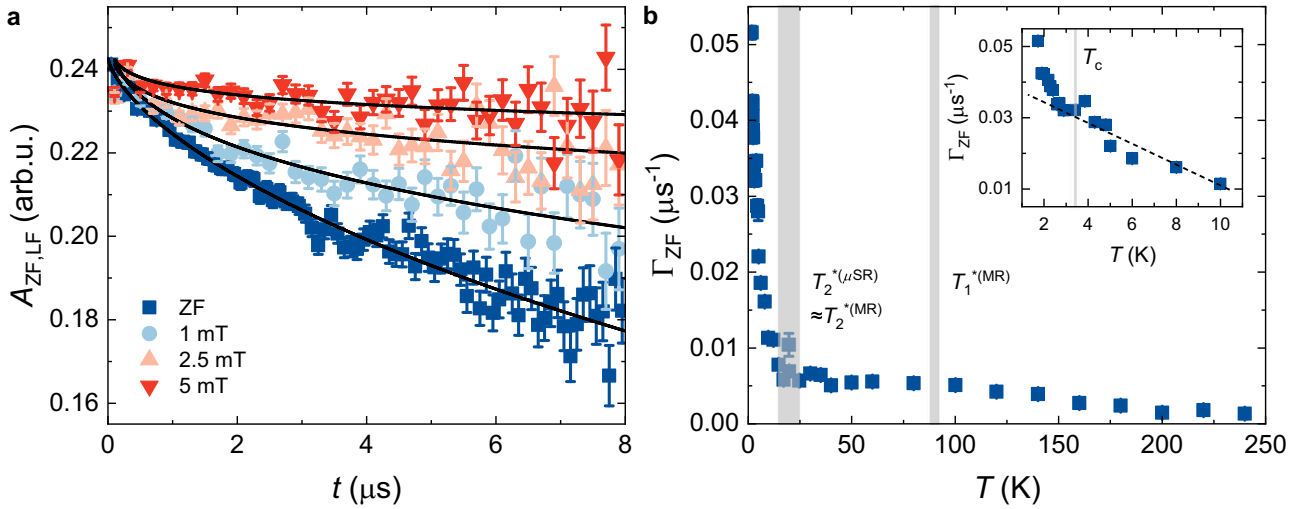

Fig. 5 | Zero-field (ZF) and longitudinal-field (LF) μSR study on YRu_3Si_2. a ZF and LF μSR time spectra recorded at 5 K. The black solid line represents a fit using a simple exponential function. Error bars are the standard error of the mean (s.e.m.) in about 10^6 events. **b** Temperature dependence of ZF muon spin relaxation rate $\Gamma_{ZF}(T)$. The error bars represent the standard deviation of the fit parameters. Vertical gray lines indicate the onset temperature $T_1^{*(MR)}$, below which MR emerges, the temperature $T_2^{*(MR)}$, below which a more pronounced increase in MR is observed, and the temperature $T_2^{*(\mu SR)}$, below which the ZF muon spin relaxation rate increases. Notably, $T_2^{*(MR)} \simeq T_2^{*(\mu SR)}$. The inset shows an additional increase in Γ_{ZF} below T_c.

indicates that the superfluid density in YRu_3Si_2 is relatively dilute and points toward an unconventional pairing mechanism.

Having established the superconducting gap structure and superfluid density in YRu_3Si_2, we now shift our focus to the normal state. A key question is whether magnetism is associated with the temperature scales T_1^* and T_2^*, identified from our transport measurements. In the following, we present results from the powerful combination of zero-field and high transverse-field μSR experiments to address this question. The zero-field (ZF)-μSR spectrum (Fig. 5a) is characterized by a weak depolarization of the muon spin ensemble, indicating no evidence of long-range-ordered magnetism in YRu_3Si_2. However, the muon spin relaxation has a clearly observable temperature dependence. Since the full polarization can be recovered by the application of a small external longitudinal magnetic field, $B_{LF} = 5$ mT, the relaxation is, therefore, due to spontaneous fields which are static on the microsecond timescale. The zero-field μSR spectra for YRu_3Si_2 were fitted using the simple exponential function $P_{ZF}(t) = \exp(-\Gamma_{ZF}t)$. Across T_1^*, there is only a change in the slope of Γ. However, a significant observation occurs as the temperature is lowered below $T_2^* \simeq 25$ K, where there is a notable increase in Γ_{ZF} (Fig. 5b). Keeping in mind that there is no structural distortion across T_2^*, we can dismiss changes in the structure as the origin for the increase in relaxation rate. Therefore, we interpret our ZF-μSR results as an indication that there is an enhanced width of internal fields sensed by the muon ensemble below $T_2^* \simeq 25$ K. The increase in Γ_{ZF} below T_2^*, measured at 1.6 K, is estimated to be $\simeq 0.045\ \mu s^{-1}$, which can be interpreted as a characteristic field strength $\Gamma_{ZF}/\gamma_\mu \simeq 0.45$ G. We note that a slight additional increase of Γ_{ZF} is observed below T_c (inset of Fig. 5b). However, this does not allow us to conclude that the superconducting state itself breaks TRS. The key observation is that the onset of the increase in Γ_{ZF} occurs already at the higher temperature T_2^*, indicating that TRS breaking sets in above T_c. This implies that internal fields are already present in the normal state, and upon entering the superconducting phase, the superconductivity interacts with these fields, slightly modifying them. Thus, in YRu_3Si_2, we can state that TRS is broken at T_2^*, i.e., at a temperature higher than T_c, and the modification of Γ_{ZF} below T_c reflects the interplay with the pre-existing internal fields. A similar situation occurs in AV_3Sb_5[8]. At ambient pressure, TRS breaking is already established in the normal state, making it impossible to determine whether the superconducting state itself breaks TRS. However, by applying hydrostatic pressure to fully suppress charge order, we were able to directly probe TRS breaking by the superconducting state. These measurements demonstrated that, once charge order is suppressed, the superconducting state indeed breaks TRS. In AV_3Sb_5, the critical pressure required to suppress charge order is within 2 GPa, within the range of μSR experiments ($p_{max} = 2$ GPa). In contrast, the pressure needed to suppress charge order in YRu_3Si_2 is expected to be significantly higher[30], which prevents us from probing with μSR whether the superconducting state alone, without charge order, breaks TRS.

To corroborate the zero-field μSR results presented above, a comprehensive set of high-field μSR experiments was conducted[39]. The temperature dependencies of the muon spin relaxation rate σ_{HTF}, measured under various magnetic fields, are shown in Fig. 6a. At the lowest applied field of 0.01 T, the relaxation rate remains nearly constant down to T_2^*, below which it exhibits a clear increase—consistent with the zero-field μSR results. The overall increase in σ_{HTF} below T_2^* is smaller than that observed in zero field, as expected. As the applied field is increased, a stronger enhancement of the relaxation rate below T_2^* is observed. At 4 T, the rate is nearly ten times larger than at 0.01 T, indicating a substantial field-induced enhancement of the magnetic response. Additionally, the increase in the rate below T_1^* becomes more pronounced, and the temperature dependence above T_1^* becomes increasingly evident. As shown in Fig. 6b, the absolute value of the increase saturates above 4 T, and the changes in the overall temperature dependence become less prominent. Notably, the muon spin relaxation rate increases across the entire sample volume (see Supplementary Fig. S5), evidencing the bulk character of the magnetic state. These measurements confirm the time-reversal symmetry-breaking nature of the phase below T_2^*, as well as the emergence of a field-induced magnetic state below T_1^*. Thus, muon spin rotation experiments reveal that the MR observed in YRu_3Si_2 originates from a hidden, weak magnetic state. A field-induced enhancement of the relaxation rate was previously observed in $LaRu_3Si_2$; however, the field dependence differs significantly between $LaRu_3Si_2$ and YRu_3Si_2, as shown in Fig. 6b. In YRu_3Si_2, the relaxation rate increases more rapidly at low fields and saturates above 4 T, whereas in $LaRu_3Si_2$, the rate continues to rise steadily up to 8 T. The characteristic temperatures T_1^* and T_2^*, determined from high-field μSR, zero-field μSR, and magnetotransport measurements,

https://doi.org/10.1038/s41467-025-67881-4

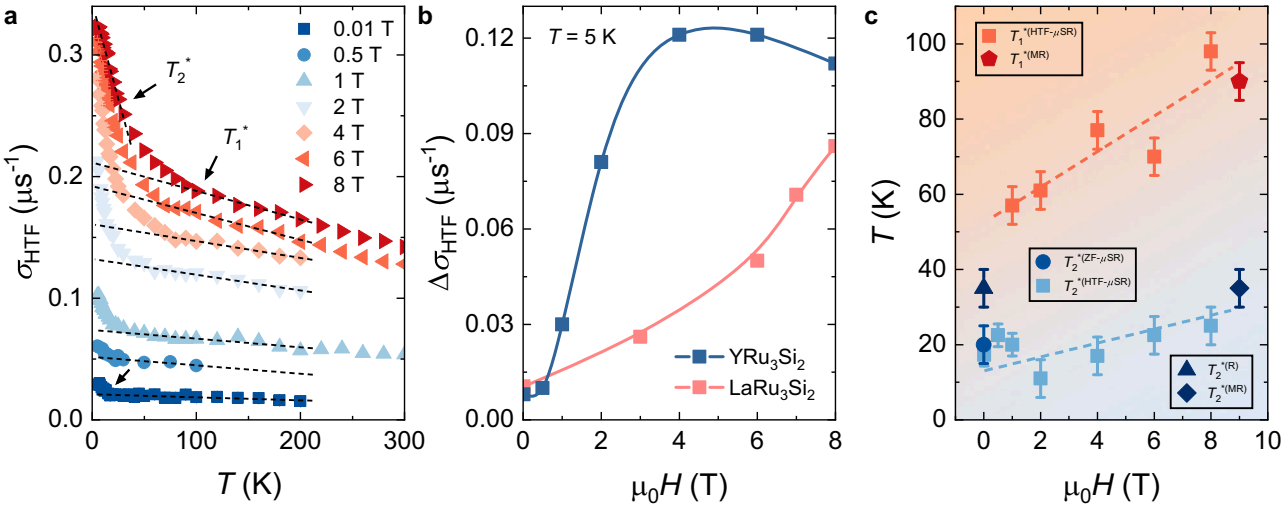

Fig. 6 | Summary of the high-field μSR study of YRu_3Si_2 in the normal state. **a** Temperature dependence of the high transverse-field (HTF) muon spin relaxation rates measured for selected external fields (dashed black lines represent the linear fit of the high-temperature data). The error bars represent the standard deviation of the fit parameters. Arrows mark the characteristic temperatures T_1^* and T_2^*. **b** The low-temperature increase in the HTF μSR rate as a function of applied magnetic field, measured at 5 K. The data reported for $LaRu_3Si_2$[29] analog are shown for comparison, as well. **c** Characteristic temperatures T_1^* and T_2^* as determined from the HTF μSR, ZF μSR, and magnetotransport measurements. Dashed lines are guides to the eye.

Table 1 | Summary of the charge order and time-reversal symmetry (TRS) breaking temperatures in kagome materials

Compound	KV_3Sb_5[9]	RbV_3Sb_5[58]	CsV_3Sb_5[59]	ScV_6Sn_6[40,60]	$LaRu_3Si_2$[29]	YRu_3Si_2 this study
T_{co} (K)	80	110	95	80	400	800
T_{ZF}^* (K)	80	110, 50	95, 30	80	35	25
T_{HF}^* (K)	80	110	95	80	80	90
$\Delta\Gamma_{ZF}$ (μs^{-1})	0.025	0.05	0.04	0.04	0.035	0.045

Comparison of the characteristic temperatures of charge order formation (T_{co}) and the temperatures below which the TRS is broken, either at zero (T_{ZF}^*) or high magnetic field (T_{HF}^*). The absolute increase in the zero-field muon spin relaxation rate below T_{ZF}^*, denoted as $\Delta\Gamma_{ZF}$, is also shown for various systems.

are summarized in Fig. 6c, showing a smooth increase with applied field. Furthermore, the continuous increase in the relaxation rate across a wide temperature range above T_1^* suggests the presence of weak magnetic correlations at elevated temperatures, potentially linked to the high-temperature charge order. To verify this, future measurements extending up to the charge-ordering temperature $T_{co} = 800$ K will be necessary. The evidence for the transition below 20 K is also provided by magnetic susceptibility measurements (see Supplementary Fig. S4). Taken together, the weak magnetism detected below T_2^* is established by a powerful combination of complementary microscopic techniques, including muon-spin rotation, resistivity, magnetoresistivity, and magnetization measurements.

Discussion

To summarize, our findings establish YRu_3Si_2 as a distinctive kagome-lattice superconductor exhibiting several remarkable properties: (1) High-temperature charge order below $T_{co} \simeq 800$ K: YRu_3Si_2 demonstrates a record-high onset temperature for charge order, characterized by a propagation vector of (1/2, 0, 0). This charge order wave vector differs from the (1/4) and (1/6) modulations observed in $LaRu_3Si_2$, but closely resembles the one reported in AV_3Sb_5 systems[3]. (2) Time-reversal symmetry-breaking phase below $T_2^* \simeq 25$ K: Between the onset of charge order and the superconducting transition, an electronically driven phase that breaks TRS emerges, indicating complex underlying electronic interactions. TRS breaking in the normal state has been reported in several charge-ordered kagome systems, including AV_3Sb_5, ScV_6Sn_6, and $LaRu_3Si_2$. Furthermore, the magnitude of the TRS-breaking signal is quite comparable across different kagome systems (see Table 1). This indicates that this phenomenon is a ubiquitous feature of the kagome lattice. However, a notable distinction emerges: in ScV_6Sn_6, the onset of TRS breaking coincides closely with the onset of charge order. In AV_3Sb_5, the onset of TRS breaking coincides with the emergence of charge order, with a stronger TRS-breaking signal developing at lower temperatures (see Table 1). In contrast, a notable difference arises in $LaRu_3Si_2$ and YRu_3Si_2, where TRS breaking sets in at temperatures well below the primary charge-ordering transition (see Table 1). (3) Field-induced magnetic response at least below $T_1^* \simeq 90$ K. (4) Band structure calculations identify a flat band and two VHSs near the Fermi level (see detailed characterization of the VHSs below), suggesting a strong interplay between electronic correlations and emergent orders. (5) Superconductivity with an unconventional gap structure: The superconducting state in YRu_3Si_2 features a gap structure consistent with either two isotropic full gaps or an anisotropic nodeless gap, suggesting unconventional pairing mechanisms. Taken together, this makes YRu_3Si_2 an ideal platform for exploring the interplay between multiple symmetry-breaking phases and their connection to superconductivity, and strongly motivates further investigations using techniques such as STM, ARPES, and beyond.

Finally, we discuss the possible origin of the observed time-reversal symmetry-breaking phase within the charge-ordered phase. Two VHSs are identified near the Fermi level in the pristine band structure, one of which lies within the flat band (Fig. 7a). These VHSs exhibit orbital characters of the out-of-plane d_{xz} and d_{yz} orbitals for VHS1 and the in-plane d_{xy} and $d_{x^2-y^2}$ orbitals for VHS2. This is reminiscent of the VHSs with both in-plane and out-of-plane orbital characters in CsV_3Sb_5 (Fig. 7c) and ScV_6Sn_6 (Fig. 7d), where time-reversal

https://doi.org/10.1038/s41467-025-67881-4

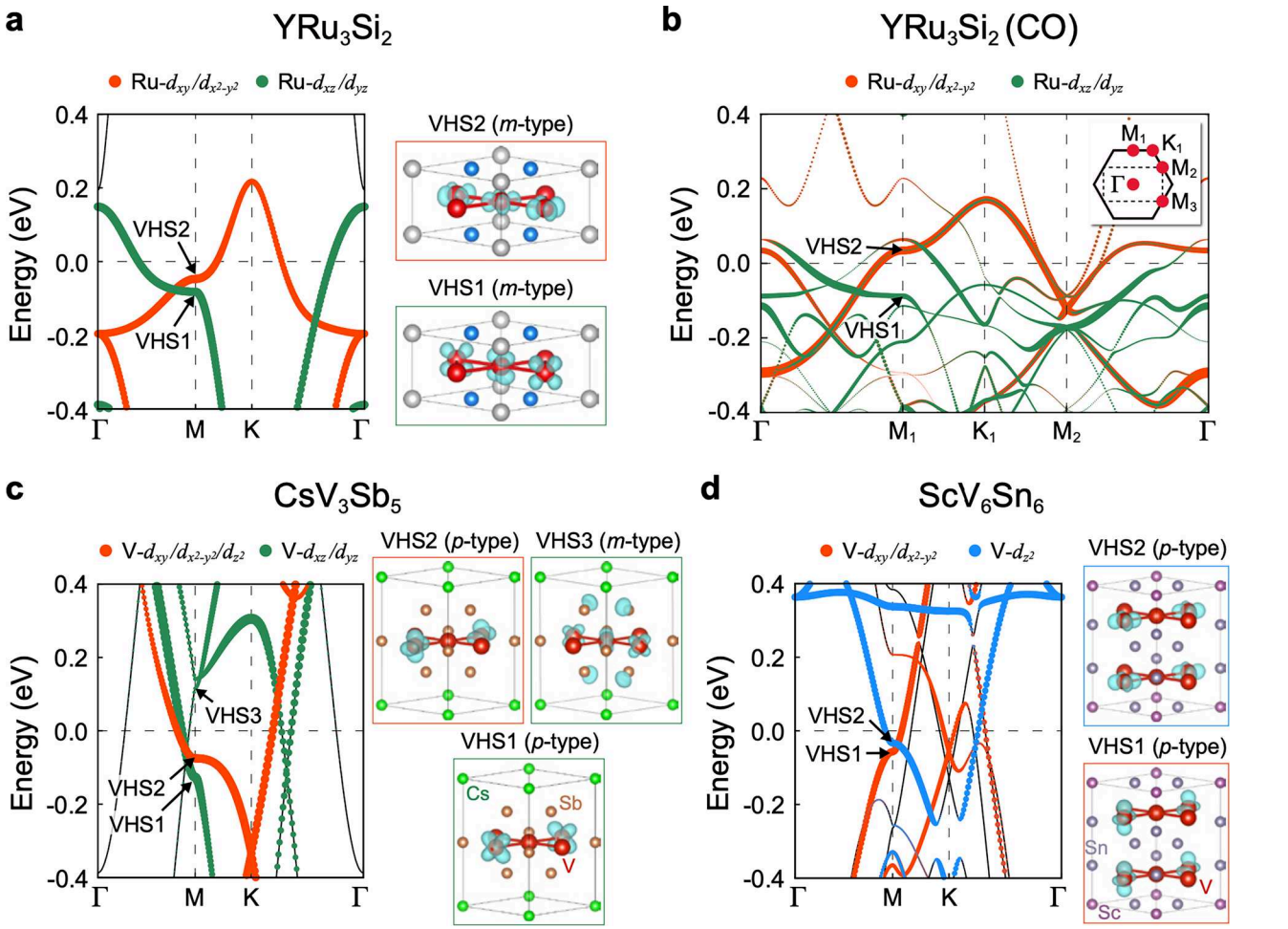

Fig. 7 | VHS physics in YRu_3Si_2. VHS points near the Fermi level and their characters for **a** YRu_3Si_2, **c** CsV_3Sb_5, and **d** ScV_6Sn_6. The band structure of the parent phase of each compound is shown, projected onto the *d* orbitals of the V or Ru atom, with the radius of the open circles proportional to the projected weight. The charge density of VHS points is displayed, where *m*-type and *p*-type refer to sublattice-mixed and sublattice-pure types, respectively. **b** Unfolded band structure of the charge-ordered phase in YRu_3Si_2. See also the band structure without band unfolding in Supplementary Fig. S2. In the inset, the solid line indicates the BZ of the parent *P6/mmm* structure, while the dashed line indicates the BZ of the charge-ordered *Pmma* structure.

symmetry-breaking orders have been reported[9,40]. Closer inspection shows that both VHSs in YRu_3Si_2 belong to sublattice-mixed type, consisting of a mixed contribution from two kagome sublattices (Fig. 7a). This is distinct from both the sublattice-mixed and sublattice-pure VHSs in CsV_3Sb_5 (Fig. 7c), as well as from the sublattice-pure VHSs in ScV_6Sn_6 (Fig. 7d). Interestingly, we reveal that the VHSs characteristics in the pristine phase are preserved in the charge-ordered state, as shown in the unfolded band structure in Fig. 7b (see also Supplementary Fig. S1 for detailed identification of the VHSs). Upon the charge order formation, the bandwidths of the two VHS bands are renormalized along the Γ–M_1–K_1 direction, positioning VHS1 (VHS2) below (above) the Fermi level at the M_1 point, while retaining their orbital characters. This is particularly remarkable, as recent theoretical studies suggest that the presence of two VHSs near the Fermi level is a key prerequisite for loop current order in kagome metals[18,41]. We thereby attribute the observed time-reversal symmetry-breaking phase within the charge-ordered phase to the persistent multiple VHSs, even under the charge order formation. YRu_3Si_2 serves as a distinct example, with different VHS characters compared to CsV_3Sb_5 and ScV_6Sn_6, which may contribute to uncovering the exact mechanism of loop current order in the kagome metal family.

We also note that the lowered symmetry of the charge-ordered state inherently gives rise to nematicity in VHS fermiology of YRu_3Si_2 (Fig. 7b). Compared to the two resilient VHSs at the M_1 point with some bandwidth renormalization, the VHSs at the M_2 point are washed out due to charge-order-driven interactions between multiple VHSs originating from the M_2 and M_3 points in the pristine BZ. This VHS fermiology is clearly distinct from the VHSs present at all three M points in the pristine phase of CsV_3Sb_5, but it is similar to the nematicity-driven lifting of VHSs, leaving VHSs only at a single M point in the charge-ordered phase of ScV_6Sn_6 below the nematic temperature[42]. The role of symmetry breaking and its impact on exotic quantum phases in kagome metals is of crucial importance, particularly in the context of VHS-driven instabilities[43,44]. Thus, YRu_3Si_2 presents itself as an intriguing kagome material for studying the interplay between VHSs and nematicity in the formation of time-reversal symmetry-breaking loop current order and superconductivity.

Methods

Sample preparation

Polycrystalline samples of YRu_3Si_2 were prepared by arc-melting from mixtures of yttrium chunks (99.9%, Thermo Scientific), ruthenium powder (99.99%, Leico), and silicon pieces (99.95%, Sigma Aldrich) under an argon atmosphere. Stoichiometric amounts of the elements were used with a 30% molar excess of ruthenium to avoid the formation of the YRu_3Si_2 phase. The ruthenium powder was pressed into pellets to avoid sputtering, and the melting process was started with the metals (yttrium and ruthenium) so that the melt

could absorb silicon. A piece of zirconium was used as a getter to remove residual oxygen. During the arc-melting process, the samples were melted and flipped several times for better homogenization. The pellets were not shiny on the surface after the synthesis; this was due to the formation of a thin oxide layer, which was mechanically removed. All of the measurements were performed on YRu_3Si_2 samples from the same batch.

First-principles calculations

We perform density functional theory (DFT) calculations using the Vienna ab initio simulation package VASP[45], implementing the projector-augmented wave method[46]. We use PAW pseudopotentials with valence configurations: $4s^24p^64d^25s^1$ for Y atoms, $4s^24p^64d^75s^1$ for Ru atoms, and $3s^23p^2$ for Si atoms. We approximate the exchange-correlation functional with the generalized-gradient approximation PBEsol[47]. We use a kinetic energy cutoff for the plane wave basis of 400 eV and a Gaussian smearing of 0.02 eV. We use Γ-centered **k**-point grids with a **k**-spacing of 0.1 Å^{-1}. For plotting the DOS, a denser **k**-point grid with a **k**-spacing of 0.04 Å^{-1} and the tetrahedron method is used. All the structures are optimized until the forces are below 0.001 eV/Å. The unfolded band structure of the charge-ordered phase is obtained using the method proposed by Popescu and Zunger[48] as implemented in the VaspBandUnfolding code[49]. We perform harmonic phonon calculations using the finite displacement method in conjunction with nondiagonal supercells[50]. The dynamical matrices are calculated on uniform **q** grids of size 6 × 6 × 6 for the high-temperature *P6/mmm* structure, and of size 2 × 2 × 2 for the *Cccm* and *Pmma* structures. We find that both the *Cccm* and *Pmma* structures are dynamically stable at the harmonic level (Supplementary Fig. S3).

Single crystal X-ray diffraction measurements

We employed both laboratory-based single-crystal X-ray diffraction (80–900 K) at the Paul Scherrer Institute and high-resolution synchrotron X-ray diffraction (10–300 K) at DESY to uncover the charge-ordered state. These diffraction techniques provide the most direct probes of structural transitions and charge order. These diffraction techniques provide the most direct probes of structural transitions and charge order. The experiments are complemented by DFT calculations, which provide microscopic insight into each state. Single crystals of YRu_3Si_2 of up to 50 µm were selected from a crushed arc-melted button, washed consequently in dilute HCl, H_2O, ethanol, and mounted on MiTeGen loops or a quartz capillary. Diffraction measurements were carried out using the laboratory STOE STADIVARI single-crystal diffractometer equipped with the micro-focused Mo K_α X-ray source and Dectris EIGER 1M 2R detector. Measurements were carried out in the temperature range between 80 and 400 K using Oxford CryoStream 800 Series and between RT and 900 K using STOE HeatStream (Ar flow of 0.8 L/min). Hard X-ray synchrotron experiments were carried out at the P21.1 beamline[51] at Petra III, DESY, using 101.6 keV photons. These measurements were done with the Dectris X 4M detector in cryogenic conditions down to 10 K and up to 300 K. Data collection and reduction, as well as reconstruction of reciprocal space, were performed using the X-Area software package [X-area package (STOE and Cie GmbH, Darmstadt, Germany, 2022)]. Structure solution and refinement were performed using Jana2020 software[52]. Similar to $LaRu_3Si_2$, the hexagonal pseudo-symmetry of the diffraction patterns (Fig. 1) is due to ortho-hexagonal twinning, which was accounted for during refinement of the lt-hex and charge-ordered phases.

Magnetotransport measurements

Magnetotransport measurements were carried out in a standard four-probe method using the Physical Property Measurement System (PPMS, Quantum Design). A well-cut, polished, rectangular-shaped thin piece was used. The diagonal arrangement of voltage contacts was used, and the magnetoresistance and Hall resistance were obtained by symmetrization and anti-symmetrization of the measured data, respectively.

Muon spin rotation experiments

Zero-field (ZF) and transverse-field (TF) μSR experiments were performed on the GPS instrument and high-field HAL-9500 instrument, equipped with BlueFors vacuum-loaded cryogen-free dilution refrigerator (DR), at the Swiss Muon Source (SμS) at the Paul Scherrer Institut, in Villigen, Switzerland.

In a μSR experiment, nearly 100 % spin-polarized muons μ^+ are implanted into the sample one at a time. The positively charged μ^+ thermalize at interstitial lattice sites, where they act as magnetic microprobes. In a magnetic material, the muon spin precesses in the local field B_μ at with the Larmor frequency $\nu_\mu = \gamma_\mu/(2\pi)B_\mu$ (muon gyromagnetic ratio $\gamma_\mu/(2\pi) = 135.5$ MHz T^{-1}). Using the μSR technique, important length scales of superconductors can be measured, namely the magnetic penetration depth λ and the coherence length ξ. If a type-II superconductor is cooled below T_c in an applied magnetic field ranging between the lower (H_{c1}) and the upper (H_{c2}) critical fields, a vortex lattice is formed, which in general is incommensurate with the crystal lattice, with vortex cores separated by much larger distances than those of the unit cell. Because the implanted muons stop at given crystallographic sites, they will randomly probe the field distribution of the vortex lattice. Such measurements need to be performed in a field applied perpendicular to the initial muon spin polarization (the so-called TF configuration).

Zero-field and high-transverse-field experiments were performed to probe normal state properties on the HAL instrument in a field range of 0.01–8 T. The sample in the form of a compressed pellet (diameter 8 mm) was placed on the silver sample holder and mounted in the cryostat.

Analysis of TF-μSR data

In order to model the asymmetric field distribution ($P(B)$) in the SC state, the TF-μSR time spectra measured below T_c are analyzed using the following two-component functional form:

$$A_{TF}(t) = \sum_{i=0}^{2} A_{s,i} \exp\left[-\frac{\sigma_i^2 t^2}{2}\right] \cos(\gamma_\mu B_{\mathrm{int},s,i} t + \varphi) \tag{2}$$

Here $A_{s,i}$, σ_i and $B_{\mathrm{int},s,i}$ is the initial asymmetry, relaxation rate, and local internal magnetic field of the ith component. φ is the initial phase of the muon-spin ensemble. $\gamma_\mu/(2\pi) \simeq 135.5$ MHz/T is the muon gyromagnetic ratio. The first and second moments of the local magnetic field distribution are given by[53]

$$\langle B \rangle = \sum_{i=0}^{2} \frac{A_{s,i} B_{\mathrm{int},s,i}}{A_{s,1} + A_{s,2}} \tag{3}$$

and

$$\langle \Delta B \rangle^2 = \frac{\sigma^2}{\gamma_\mu^2} = \sum_{i=0}^{2} \frac{A_{s,i}}{A_{s,1} + A_{s,2}} \left[\sigma_i^2/\gamma_\mu^2 + (B_{\mathrm{int},s,i} - \langle B \rangle)^2\right]. \tag{4}$$

Above T_c, in the normal state, the symmetric field distribution could be nicely modeled by only one component. The obtained relaxation rate and internal magnetic field are denoted by σ_{ns} and $B_{\mathrm{int},s,ns}$. σ_{ns} is found to be small and temperature independent (dominated by nuclear magnetic moments) above T_c and assumed to be constant in the whole temperature range. Below T_c, in the SC state, the relaxation rate and internal magnetic field are indicated by σ_{SC} and $B_{\mathrm{int},s,sc}$. σ_{SC} is extracted by using $\sigma_{SC} = \sqrt{\sigma^2 - \sigma_{ns}^2}$. $B_{\mathrm{int},s,sc}$ is evaluated from $\langle B \rangle$ using Eq. (3).

Analysis of $\lambda(T)$

$\lambda(T)$ was calculated within the local (London) approximation ($\lambda \gg \xi$) by the following expression[54,55]:

$$\frac{\sigma_{SC}(T,\Delta_{0,i})}{\sigma_{SC}(0,\Delta_{0,i})} = 1 + \frac{1}{\pi}\int_0^{2\pi}\int_{\Delta(T,\varphi)}^{\infty}\left(\frac{\partial f}{\partial E}\right)\frac{EdEd\varphi}{\sqrt{E^2-\Delta_i(T,\varphi)^2}}, \quad (5)$$

where $f = [1 + \exp(E/k_BT)]^{-1}$ is the Fermi function, φ is the angle along the Fermi surface, and $\Delta_i(T,\varphi) = \Delta_{0,i}\Gamma(T/T_c)g(\varphi)$ ($\Delta_{0,i}$ is the maximum gap value at $T = 0$). The temperature dependence of the gap is approximated by the expression $\Gamma(T/T_c) = \tanh\{1.82[1.018(T_c/T-1)]^{0.51}\}$,[56] while $g(\varphi)$ describes the angular dependence of the gap and is replaced by 1 for both a single isotropic gap and and two isotropic full gaps, and $|\cos(2\varphi)|$ for a nodal d wave gap[57].

Data availability

All the results are available from the authors upon request.

References

1. Keimer, B., Kivelson, S., Norman, M., Uchida, S. & Zaanen, J. From quantum matter to high-temperature superconductivity in copper oxides. *Nature* **518**, 179–186 (2015).
2. Syozi, I. Statistics of kagome lattice. *Prog. Theor. Phys.* **6**, 306 (1951).
3. Wilson, S. D. & Ortiz, B. R. AV_3Sb_5. Kagome superconductors. *Nat. Rev. Mater.* **9**, 420–432 (2024).
4. Ortiz, B. R. et al. New kagome prototype materials: discovery of KV_3Sb_5, RbV_3Sb_5, and CsV_3Sb_5. *Phys. Rev. Mater.* **3**, 094407 (2019).
5. Ortiz, B. R. et al. CsV_3Sb_5: a Z_2 topological kagome metal with a superconducting ground state. *Phys. Rev. Lett.* **125**, 247002 (2020).
6. Denner, M. M., Thomale, R. & Neupert, T. Analysis of charge order in the kagome metal AV_3Sb_5 (*A* = K, Rb, Cs). *Phys. Rev. Lett.* **127**, 217601 (2021).
7. Yin, J.-X., Lian, B. & Hasan, M. Z. Topological kagome magnets and superconductors. *Nature* **612**, 647–657 (2022).
8. Guguchia, Z., Khasanov, R. & Luetkens, H. Unconventional charge order and superconductivity in kagome-lattice systems as seen by muon-spin rotation. *npj Quantum Mater.* **8**, 41 (2023).
9. Mielke III, C. et al. Time-reversal symmetry-breaking charge order in a kagome superconductor. *Nature* **602**, 245–250 (2022).
10. Plokhikh, I. et al. Discovery of charge order above room-temperature in the prototypical kagome superconductor $La(Ru_{1-x}Fe_x)_3Si_2$. *Commun. Phys.* **7**, 182 (2024).
11. Neupert, T., Denner, M. M., Yin, J.-X., Thomale, R. & Hasan, M. Z. Charge order and superconductivity in kagome materials. *Nat. Phys.* **18**, 137–143 (2022).
12. Deng, H. et al. Evidence for time-reversal symmetry-breaking kagome superconductivity. *Nat. Mater.* 1–6 (2024).
13. Wagner, G., Guo, C., Moll, P. J. W., Neupert, T. & Fischer, M. H. Phenomenology of bond and flux orders in kagome metals. *Phys. Rev. B* **108**, 125136 (2023).
14. Kiesel, M. L., Platt, C. & Thomale, R. Unconventional fermi surface instabilities in the kagome Hubbard model. *Phys. Rev. Lett.* **110**, 126405 (2013).
15. Teng, X. et al. Discovery of charge density wave in a kagome lattice antiferromagnet. *Nature* **609**, 490–495 (2022).
16. Liu, Y. et al. Superconductivity under pressure in a chromium-based kagome metal. *Nature* **632**, 1032–1037 (2024).
17. Yang, H. et al. Superconductivity and nematic order in a new titanium-based kagome metal $CsTi_3Bi_5$ without charge density wave order. *Nature Communications* **15**, 9626 (2024).
18. Christensen, M. H., Birol, T., Andersen, B. M. & Fernandes, R. M. Loop currents in AV_3Sb_5 kagome metals: multipolar and toroidal magnetic orders. *Phys. Rev. B* **106**, 144504 (2022).
19. Guo, C. et al. Switchable chiral transport in charge-ordered kagome metal CsV_3Sb_5. *Nature* **611**, 461–466 (2022).
20. Bonfà, P. et al. Unveiling the nature of electronic transitions in RbV_3Sb_5 with avoided level crossing *μSR*. *Phys. Rev. Research* **7**, L032046 (2025).
21. Wang, K., Chen, S., Kim, S.-W. & Monserrat, B. Origin of competing charge density waves in kagome metal ScV_6Sn_6. *Nat. Commun.* **15**, 10428 (2024).
22. Dong, J.-W., Wang, Z. & Zhou, S. Loop-current charge density wave driven by long-range Coulomb repulsion on the kagomé lattice. *Phys. Rev. B* **107**, 045127 (2023).
23. Graham, J. N. et al. Microscopic probing of the superconducting and normal state properties of $Ta_2V_{3.1}Si_{0.9}$ by muon spin rotation. *Commun. Mater.* **5**, 225 (2024).
24. Xu, Y. et al. Three-state nematicity and magneto-optical Kerr effect in the charge density waves in kagome superconductors. *Nat. Phys.* **18**, 1470–1475 (2022).
25. Ingham, J., Thomale, R. & Scammell, H. D. Vestigial order from an excitonic mother state in kagome superconductors AV_3Sb_5. arXiv preprint arXiv:2503.02929 (2025).
26. Scammell, H. D., Ingham, J., Li, T. & Sushkov, O. P. Chiral excitonic order from twofold van Hove singularities in kagome metals. *Nat. Commun.* **14**, 605 (2023).
27. Vandenberg, J. M. & Barz, H. The crystal structure of a new ternary silicide in the system rare-earth–ruthenium–silicon. *Mater. Res. Bull.* **15**, 1493–1498 (1980).
28. Mielke III, C. et al. Nodeless kagome superconductivity in $LaRu_3Si_2$. *Phys. Rev. Mater.* **5**, 034803 (2021).
29. Mielke III, C. et al. Coexisting multiple charge orders and magnetism in the kagome superconductor $LaRu_3Si_2$. *Adv. Mater.* **37**, 2503065 (2025).
30. Ma, K. et al. Correlation between the dome-shaped superconducting phase diagram, charge order, and normal-state electronic properties in $LaRu_3Si_2$. *Nat. Commun.* **16**, 6149 (2025).
31. Misawa, R. et al. Chemical enhancement of superconductivity in $LaRu_3Si_2$ with mode-selective coupling between kagome phonons and flat bands. *Phys. Rev. Res.* **7**, 033032 (2025).
32. Deng, J. et al. Theory of superconductivity in $LaRu_3Si_2$ and predictions of new kagome flat band superconductors. arXiv preprint arXiv:2503.20867 (2025).
33. Li, Z. et al. Superconducting dome and structural changes in $LaRu_3Si_2$ under pressure. *Phys. Rev. B* **111**, 144505 (2025).
34. Gong, C. et al. Superconductivity in kagome metal YRu_3Si_2 with strong electron correlations. *Chin. Phys. Lett.* **39**, 087401 (2022).
35. Brandt, E. Flux distribution and penetration depth measured by muon spin rotation in high-T_c superconductors. *Phys. Rev. B* **37**, 2349 (1988).
36. Mielke III, C. et al. Local spectroscopic evidence for a nodeless magnetic kagome superconductor $CeRu_2$. *J. Phys.: Condens. Matter* **34**, 485601 (2022).
37. Ushioda, T. & Muranaka, T. Two-gap superconducting states of $LaRu_3Si_2$. *Physica C* **625**, 1354583 (2024).
38. Uemura, Y. et al. Universal correlations between T_c and n_s/m*(carrier density over effective mass) in high-T_c cuprate superconductors. *Phys. Rev. Lett.* **62**, 2317 (1989).
39. Sedlak, K., Scheuermann, R., Stoykov, A. & Amato, A. Geant4 simulation and optimisation of the high-field *μSR* spectrometer. *Physica B* **404**, 970–973 (2009).
40. Guguchia, Z. et al. Hidden magnetism uncovered in a charge ordered bilayer kagome material ScV_6Sn_6. *Nat. Commun.* **14**, 7796 (2023).
41. Li, H., Kim, Y. B. & Kee, H.-Y. Intertwined van Hove singularities as a mechanism for loop current order in kagome metals. *Phys. Rev. Lett.* **132**, 146501 (2024).

42. Jiang, Y.-X. et al. Van Hove annihilation and nematic instability on a kagome lattice. *Nat. Mater.* **23**, 1214–1221 (2024).
43. Kim, S.-W., Oh, H., Moon, E.-G. & Kim, Y. Monolayer kagome metals AV_3Sb_5. *Nat. Commun.* **14**, 591 (2023).
44. Guo, C. et al. Correlated order at the tipping point in the kagome metal CsV_3Sb_5. *Nat. Phys.* **20**, 579–584 (2024).
45. Kresse, G. & Furthmüller, J. Efficient iterative schemes for ab initio total-energy calculations using a plane-wave basis set. *Phys. Rev. B* **54**, 11169–11186 (1996).
46. Blöchl, P. E. Projector augmented-wave method. *Phys. Rev. B* **50**, 17953–17979 (1994).
47. Perdew, J. P. et al. Restoring the density-gradient expansion for exchange in solids and surfaces. *Phys. Rev. Lett.* **100**, 136406 (2008).
48. Popescu, V. & Zunger, A. Extracting *E* versus *k* effective band structure from supercell calculations on alloys and impurities. *Phys. Rev. B* **85**, 085201 (2012).
49. Zheng, Q. *VaspBandUnfolding* https://github.com/QijingZheng/VaspBandUnfolding(2018).
50. Lloyd-Williams, J. H. & Monserrat, B. Lattice dynamics and electron–phonon coupling calculations using nondiagonal supercells. *Phys. Rev. B* **92**, 184301 (2015).
51. Zimmermann, M. V. et al. P21.1 at PETRA III—a high-energy X-ray diffraction beamline for physics and chemistry. *J. Synchrotron Radiat.* **32**, 802–814 (2025).
52. Petr^íček, V., Palatinus, L., Plášil, J. & Dušek, M. Jana 2020—a new version of the crystallographic computing system Jana. *Z. Kristallogr.—Cryst. Mater.* **238**, 271–282 (2023).
53. Khasanov, R. et al. Magnetic penetration depth in $RbOs_2O_6$ studied by muon spin rotation. *Phys. Rev. B* **72**, 104504 (2005).
54. Suter, A. & Wojek, B. Musrfit: a free platform-independent framework for μSR data analysis. *Phys. Procedia* **30**, 69 (2012).
55. Tinkham, M. *Introduction to Superconductivity* 2nd edn (Dover Publications, 2004).
56. Carrington, A. & Manzano, F. Magnetic penetration depth of MgB_2. *Physica C* **385**, 205 (2003).
57. Guguchia, Z. et al. Direct evidence for a pressure-induced nodal superconducting gap in the $Ba_{0.65}Rb_{0.35}Fe_2As_2$ superconductor. *Nat. Commun.* **6**, 8863 (2015).
58. Guguchia, Z. et al. Tunable unconventional kagome superconductivity in charge ordered RbV_3Sb_5 and KV_3Sb_5. *Nat. Commun.* **14**, 153 (2023).
59. Khasanov, R. et al. Time-reversal symmetry broken by charge order in CsV_3Sb_5. *Phys. Rev. Res.* **4**, 023244 (2022).
60. Arachchige, H. W. S. et al. Charge density wave in kagome lattice intermetallic ScV_6Sn_6. *Phys. Rev. Lett.* **129**, 216402 (2022).

Acknowledgements

The μSR experiments were carried out at the Swiss Muon Source (SμS) Paul Scherrer Insitute, Villigen, Switzerland. Z.G. acknowledges support from the Swiss National Science Foundation (SNSF) through SNSF Starting Grant (No. TMSGI2_211750). Z.G. acknowledges the useful discussions with Dr. Robert Scheuermann. S.-W.K. acknowledges support from a Leverhulme Trust Early Career Fellowship (ECF-2024-052). K.W., B.M., and S.-W.K. acknowledge support from a UKRI Future Leaders Fellowship [MR/V023926/1]. I.P. acknowledges support from the Paul Scherrer Institute research grant no. 2021 01346. The computational resources were provided by the Cambridge Tier-2 system operated by the University of Cambridge Research Computing Service and funded by EPSRC [EP/P020259/1], and by the UK National Supercomputing Service ARCHER2, for which access was obtained via the UKCP consortium and funded by EPSRC [EP/X035891/1]. Z.W. is supported by the U.S. Department of Energy, Basic Energy Sciences Grant DE-FG02-99ER45747. L.M., J.O., and I.B. acknowledge support from UZH Grants project numbers FK-23-128, K-22-095, and FK-23-113. Part of this research was conducted at the P21.1 beamline at DESY, a member of the Helmholtz Association (HGF). We would like to thank Fernando Igoa for their technical assistance during the experiment.

Author contributions

Z.G. conceived, designed, and supervised the project. Density functional theory calculations: S.-W.K., K.W., and B.M. Sample growth: A.L., M.Sa., and F.v.R. Magnetotransport experiments: V.S. and Z.G. Magnetization experiments: P.K. and Z.G. Laboratory X-ray diffraction experiments: I.P., D.G., and Z.G. X-ray diffraction experiments at DESY and corresponding analysis: P.K., O.G., I.B., L.M., J.O., M.Sp. M.V.Z., J.C., and Z.G. Muon spin rotation experiments, analysis, and corresponding discussions: Z.G., P.K., J.N.G., V.S., O.G., S.S.I., A.D., H.L., R.K., J.-X. Yin, and Z.W. Figure development and writing of the paper: Z.G., P.K., S.-W.K., with contributions from all authors. All authors discussed the results, interpretation, and conclusion.

Competing interests

The authors declare no competing interests.

Additional information

Supplementary information The online version contains supplementary material available at https://doi.org/10.1038/s41467-025-67881-4.

Correspondence and requests for materials should be addressed to S.-W. Kim or Z. Guguchia.

Peer review information *Nature Communications* thanks Chao Cao, and the other, anonymous, reviewer(s) for their contribution to the peer review of this work. A peer review file is available.